# Enhanced visible-light activities of porous BiFeO₃ by coupling with nanocrystalline TiO₂ and mechanism

Muhammad Humayun, Amir Zada, Zhijun Li, Mingzheng Xie, Xuliang Zhang, Yang Qu, Fazal Raziq, Liqiang Jing*

*Key Laboratory of Functional Inorganic Materials Chemistry (Heilongjiang University), Ministry of Education, School of Chemistry and Materials Science, Harbin 150080, PR China*

## ABSTRACT

In this work, different mole ratio percentage of nanocrystalline anatase TiO₂/porous nanosized BiFeO₃ (T/P-BFO) nanocomposites with effective contacts have been fabricated by putting the as-prepared P-BFO into the TiO₂ sol, followed by drying at 80 °C and then calcining at 450 °C for 2 h. The photoactivities of the obtained products for pollutant degradation and H₂ evolution were measured. It is clearly demonstrated by means of the steady-state surface photo-voltage spectra, the transient-state surface photovoltage responses, and the photoluminescence spectra that the photogenerated charge carriers in the T/P-BFO nanocomposites with a proper mole ratio percentage of TiO₂ (9%) display much long lifetime and high separation in comparison to the resulting P-BFO alone. This is well responsible for the enhanced activities for degrading gas-phase acetyldehyde, the liquid-phase phenol, and for producing H₂ under visible-light irradiation. Based on the measurements of formed hydroxyl radical amount and photoelectrochemical behavior, it is suggested that the improved separation of photogenerated charges in the fabricated T/P-BFO nanocomposite is mainly attributed to the spatial transfer of visible-light-excited ($\lambda \le 500$ nm) high-energy electrons of P-BFO to TiO₂. This work will provide a feasible route to enhance the photoactivities of visible-light responsive oxide composites as photocatalysts for efficient solar energy utilization.

© 2015 Elsevier B.V. All rights reserved.

## 1. Introduction

To effectively address the consumption of fossil fuels, severe energy crises and serious environmental issues, modern society has been searching for renewable, low cost, and clean form of energy which will be used as an alternative source to fossil fuels. In this regard, photocatalytic degradation of pollutants and photocatalytic water splitting using solar energy to generate hydrogen offer a clean and environmentally friendly process [1]. Multiferroic materials have recently been used for applications in both photocatalysis and photovoltaics due to their narrow energy band gaps and ferroelectric properties, which allow them to absorb majority of the light in visible region. As a potential candidate for both pollutants degradation and water splitting, BiFeO₃ has attracted greater attention. Due to its high chemical stability, narrow band gap (2.0–2.7 eV), ferroelectric and ferromagnetic properties, BFO has been regarded as one of the third-generation visible-light responsive photocatalyst [2–5]. The ferroelectric properties of BFO with spontaneous

polarization lead to the band bending that transports the photoinduced charge carriers (electrons and holes) in opposite directions, which enhances the reactivity and separation efficiency of the photo-generated charges [6]. However, the photocatalytic efficiency of BFO is still limited due to its low conduction band position compared to the hydrogen (or O₂) reduction level [7], and usually small surface areas for catalytic reactions.

To overcome these shortfalls and to improve the photocatalytic performance of BFO, elemental doping, fabricating with semiconductor metal oxides and synthesis of porous perovskite oxides with larger surface area are highly desirable [8–11]. As we know that, catalysis belongs to the class of surface reaction and there should be a good contact between the catalyst's surface and the substrates [12]. Moreover, the nanoparticles having no pores, the reaction takes place only on the external surface, limiting the catalytic performance of the material. To overcome this, the use of porous nanomaterials would be helpful, since porous material would absorb the reactants both on the surface and inside the pores, improving the contact area and hence the catalytic performances [13–15].

In addition, to improve the photocatalytic performance of BFO and to prolong the lifetime of the photogenerated charges and

---

hence promote its separation, the construction of heterojunctional nanocomposites are widely used [16]. Zhang et al. [7] have fabricated BFO with TiO$_2$ by a pulsed laser deposition method. They investigated that titania can be made photochemically active under visible light with a wavelength of 460 nm by supporting on BFO substrate. Yang et al. [17] have fabricated one dimensional TiO$_2$ and BFO nanofibres by an electrospinning technique. They investigated that BFO/T nanocomposites exhibit high photocatalytic activity for degrading methylene blue under visible light irradiation, due to the excellent charge separation properties of the heterojunction formed between BFO and TiO$_2$. Further, the BFO/T nanofibres could be easily recycled without decrease in the photocatalytic performance due to large length to diameter ratio of the nanofibres. Recently Zhu and his co-workers [18] have fabricated BFO/TiO$_2$-NTs covered Ti electrode by ultrasonic immersion method. They demonstrated that under visible light irradiation, the BFO/TiO$_2$-NTs composites (grown on Ti sheet) exhibit significant photo-conversion efficiency than the unmodified TiO$_2$-NTs/Ti electrodes. This visible light enhanced photoelectrocatalytic efficiency for degrading rhodamine B is mainly attributed to the prolonged lifetime of the photogenerated charges via the applied bias and wider spectral response promoted by BFO. Thus, it is acceptable that the visible-light photoactivity of TiO$_2$ would be enhanced by coupling with a certain amount of BFO.

To the best of our knowledge, there is no previous report on the fabrication of nanocrystalline TiO$_2$-coupled porous BFO as efficient photocatalysts. In general case, due to the low CB position of P-BFO than TiO$_2$, the photogenerated electrons cannot be transferred to the CB of TiO$_2$. However, when a heterojunction is formed between TiO$_2$ and P-BFO, their Fermi levels tend to descend and rise up, respectively, since the Fermi level of TiO$_2$ is more negative than that of P-BFO. At the same time, an electric field is formed at the interface of the heterojunction nanocomposites. At equilibrium, the TiO$_2$ junction face becomes more positive than that of P-BFO. Thus, the visible-light excited electrons, especially for produced high-level ones, could transfer thermodynamically from the CB of BFO to TiO$_2$. It is worthy of noting, that it has been primarily demonstrated in our group that the visible-light photoactivities of Fe$_2$O$_3$ and BiVO$_4$ could be greatly improved after coupling with a proper amount of nanocrystalline TiO$_2$ [16,19]. Hence, it is feasible to couple TiO$_2$ with P-BFO for effective solar energy utilization.

Herein, P-BFO and T/P-BFO nanocomposites have been successfully prepared. It is demonstrated that the lifetime of photogenerated charge carriers of P-BFO could be prolonged by approximately millisecond timescales after a proper mole ratio percentage (9%) of TiO$_2$ is coupled, corresponding to the promoted charge separation. This promoted charge separation is responsible for the visible-light enhanced photocatalytic activities for pollutant degradation and water reduction. Moreover, it is suggested for the first time that the prolonged life-time and promoted separation of photogenerated charges in the fabricated T/P-BFO nanocomposites are attributed to the unusual spatial transfer of visible-light-excited ($\lambda \leq 500$ nm) high-energy electrons of P-BFO to TiO$_2$. This work will provide a feasible route to synthesize BFO-based nanophotocatalysts for efficient solar energy utilization, which is also applicable to other visible-light-responsive semiconducting composite nanomaterials.

## 2. Experimental

### 2.1. Chemicals and reagents

All the reagents were of analytical grade and used as-received without further purification. Deionized water was used throughout the reaction.

### 2.2. Synthesis of photocatalyst

#### 2.2.1. Synthesis of P-BFO

Nanocrystalline P-BFO was synthesized by taking equimolar (0.04 M) amounts of Bi(NO$_3$)$_3$·5H$_2$O (19.4 g) and Fe(NO$_3$)$_3$·9H$_2$O (16.16 g) and dissolved in a beaker containing (30–50 vol%) of ethylene glycol and methanol. Then PS colloidal crystals were soaked in the metal precursor solution for 2 h. The solution was kept under stirring for 3 h. After that the solution was heated in a convection oven at 150 °C, until all the liquids were evaporated. To remove PS spheres, the obtained brown powder was calcined at 400 °C at a temp ramp of 1 °C/min. The powder was then calcined at 600 °C for 2 h at temp ramp of 5 °C/min to obtain nanocrystalline P-BFO.

#### 2.2.2. Synthesis of T/P-BFO

To fabricate various samples of T/P-BFO nanocomposite powders, for each sample 2 g freshly prepared P-BFO was taken and dissolved into a mixed solution containing 10 mL water, 40 mL anhydrous ethanol, and 2 mL HNO$_3$ (68%), under stirring at room temperature. Then as-prepared solutions were ultrasonically treated for 1 h followed by vigorous magnetic stirring for 2 h. After that, 1:9 by volume of Ti(OBu)$_4$ solution was prepared by taking 10 mL of Ti(OBu)$_4$ and dissolved in 90 mL of anhydrous ethanol. The solution was then kept under continuous magnetic stirring for 1 h. From this stock solution, various molar ratio (i.e 3 mL, 6 mL, 9 mL and 12 mL) was added to the as-weighted (2 g) of the P-BFO samples and the mixture was stirred for 6 h. The reaction mixture was then dried in a convection oven at 85 °C, and finally calcined at 450 °C in air for 2 h. Different mole ratios of T/P-BFO nanocomposites were obtained. The nanocomposites were denoted by XT/P-BFO; in which X represent the mole ratio percentage of Ti to P-BFO.

### 2.3. Characterization

The materials were characterized by using various techniques. The crystal structures of the samples were determined with the help of XRD (Rigaku D/MAX-rA powder diffractometer, Japan), using Cu Kα radiation ($\alpha = 0.15418$ nm), at an accelerating voltage of 30 kV, and emission current of 20 mA was employed. Transmission electron microscope (TEM) JEOL JEM-2010 at an accelerating voltage of 200 kV was used to record the electron micrographs of the samples. FT-IR spectra of the samples were collected with a Bruker Equinox 55 spectrometer, using KBr as diluents. The UV–vis diffuse reflection spectra (UV–vis DRS) of the samples were recorded with Shimadzu UV-2550 Spectrophotometer, using BaSO$_4$ as a reference. The N$_2$ adsorption–desorption isotherm of various samples were carried out by Micromeritics ASAP 2020 M system at the temperature of liquid nitrogen, while keeping the system out-gassed for 10 h at 300 °C prior to measurements. ST-2000 constant volume adsorption apparatus was used for the evaluation of BET surface area. The atmosphere-controlled SS-SPS measurement for samples was carried out with a home-built apparatus, equipped with a lock-in amplifier (SR830) synchronized with a light chopper (SR540). The powder sample was sandwiched between two indium tin oxide (ITO) glass electrodes, which were arranged in an atmosphere-controlled container with a quartz window, and a monochromatic light was obtained by passing light from a 500 W xenon lamp (CHF XQ500W, Global xenon lamp power) through a double prism monochromator (SBP300). TS-SPV measurements for samples was collected by the process that the sample chamber connected an ITO glass as top electrode and a steel substrate as bottom electrode, and a 10 μm thick mica spacer was placed between the ITO glass and the sample to decrease the space charge region at the ITO-sample interface. The samples were excited by a radiation pulse of 532 nm with 10 ns width from the second harmonic of a neodymium-doped

yttrium aluminum garnet (Nd:YAG) laser (Lab-130-10H, Newport, Co.). Intensity of the pulse was measured by a high-energy pyro-electric sensor (PE50BF-DIF-C, Ophir Photonics Group). The signals were amplified with a pre-amplier and then registered by a 1 GHz digital phosphor oscilloscope (DPO 4104B, Tektronix). The TS-TPV measurements were performed in air atmosphere at room temperature. The photo luminescence (PL) spectra of the samples were measured with a PE LS 55 spectrofluorophotometer at excitation wavelength of 325 nm.

## 2.4. Photoelectrochemical measurements

To study the photoelectrochemistry of the as-prepared T/P-BFO nanocomposites, following operations were performed. (1) 0.05 g of the as-synthesized T/P-BFO nanocomposites powder was dispersed in 2 mL of isopropyl alcohol and ultrasonically treated for 1 h followed by vigorous magnetic stirring for 1 h. (2) To the reaction mixture, 0.05 g of Macrogol-6000 was added, and re-treated by ultrasonic process for 1 h followed by continuous magnetic stirring for 1 h. (3) Finally 0.05 mL of acetylacetone was added to the reaction mixture and followed by an ultrasonic treatment and vigorous magnetic stirring for 96 h. (4) Conductive fluorine-doped tin oxide (FTO)-coated glasses were cleaned by ultrasonication in acetone for 1 h and then followed by deionized water. The FTO coated glasses were dried in air for 20 min, and then sintered at 450 °C for 30 min prior to use. These FTO coated glasses were used as substrates for the T/P-BFO nanocomposite films. The nanocomposite films were prepared by the doctor blade method using Scotch tape as the spacer. The nanocomposite films were dried in air for 20 min, and then sintered at 450 °C for 30 min. When room temperature was attained, the FTO coated glasses with paste of nanocomposite films were cut into 1.0 cm × 3.0 cm pieces having a nanocomposite film surface area of 1.0 cm × 1.0 cm. To prepare a photoelectrode, an electrical contact was made with FTO substrate by using a silver conducting paste connected to a copper wire, and then enclosed in a glass tube. The working geometric surface area of nanocomposites was 0.5 cm × 0.5 cm whereas the remaining area was covered with epoxy resin.

## 2.5. Evaluation of photocatalytic activity for pollutant degradation

To evaluate the photocatalytic performance of various samples, liquid phase phenol and gas phase acetaldehyde were chosen as model pollutants, because of their harmful effect to human health and natural environment. Both are widely produced as by-product in industrial synthesis. The photocatalytic experiments for phenol were carried out in a 100 mL of glass reactor, and the radiation source was a 150 W GYZ220 high-pressure Xenon lamp (made in China) with a cut-off filter (λ > 420 nm). To measure the photocatalytic activity, for each measurement 0.1 g of photocatalyst was taken and dissolved in 80 mL of 10 mg/L phenol solution under stirring for 1 h to reach the adsorption saturation and then irradiated for 1 h. After every 1 h photocatalytic reaction, the samples were centrifuged and the phenol concentration was analyzed by the colorimetric method of 4-aminoantipyrine at the characteristic optical adsorption of 510 nm with a Model Shimadzu UV2550 spectrophotometer. To evaluate the photocatalytic activities of gas-phase acetaldehyde, in a typical experiment, the light source was a xenon lamp (XQ150/150 W, Warren Bulb Factory, Shanghai) whose emitting spectrum was similar to sunlight, and to cut off the UV-light (<420 nm), a light filter was placed between the source of light and the reactor. For each experiment, 0.05 g of powder sample was taken in the ceramic pot and kept in a pyrex glass cylinder reactor with a volume of 640 mL and diameter of 7.0 cm respectively. A mixture of gas containing $O_2$ (20%) and acetaldehyde (80%) was

introduced to pass through the reactor, and initial concentration of the acetaldehyde gas was kept 810 ppm. Prior to irradiation, the reactor containing mixed gas was kept in the dark for 30 min to attain the adsorption–desorption equilibrium. The concentration of acetaldehyde gas was measured at 30 min intervals with a gas chromatograph (GC- 2014, SHIMADZU) equipped with a flame ionization detector. After that, visible-light was fall on the reactor for 1 h and the concentration of the acetaldehyde gas was re-measured. The same experiment was repeated for every sample.

## 2.6. Evaluation of photocatalytic activity for $H_2$ evolution

Prior to $H_2$ evolution, P-BFO and T/P-BFO nanocomposites were loaded with 1 wt% Pt by an insitu photo-deposition method using aqueous solution of $H_2PtCl_6$. In a typical reaction, 0.1 g of photocatalyst was suspended in a mixture of methanol (20 mL), distilled water (80 mL), and $H_2PtCl_6$ solution (0.25, 0.01 mol L$^{-1}$) under continuous magnetic stirring. The reaction mixture was vacuumed to remove $O_2$ dissolved in water, and then irradiated by a xenon lamp (300 W) with a cutoff filter (λ > 420 nm) for 3 h. $H_2$ gas evolution was detected under visible-light irradiation, being analyzed by an inline gas chromatograph (TCD, SP7800, molecular sieve 5 Å, $N_2$ carrier, Beijing Keruida Limited).

## 2.7. Measurement of formed hydroxyl radical (•OH) amount

To detect the amount of hydroxyl radical, 50 mg sample and 20 mL 5 mg/L$^{-1}$ coumarin aqueous solution were mixed in a 50 mL of quartz reactor. The reaction mixture was irradiated by a high-pressure Xenon lamp (150 W) with a cutoff filter (λ > 420 nm) placed at about 10 cm from the reactor under continuous magnetic stirring for 1 h. Finally, a certain amount of the solution was transferred into a Pyrex glass cell for the fluorescence measurement of 7-hydroxycoumarin at the excitation wavelength of 350 nm.

## 3. Results and discussion

### 3.1. Structural Characterization and morphology

SFig. 1A shows the XRD patterns of the as-synthesized P-BFO, $TiO_2$, and T/P-BFO nanocomposites. It is confirmed that the diffraction peaks of $TiO_2$ are ascribed to the anatase phase (JCPDS Card No. 21-1272) [17]. For P-BFO calcined at 600 °C, all the diffraction patterns can be assigned to the rhombohedrally distorted perovskite phase $BiFeO_3$ (JCPDS Card No. 20-0169) [20]. In the XRD patterns of T/P-BFO nanocomposites calcined at 450 °C, no impurity peaks can be observed except for T and BFO phases. In addition, the relative peak intensity of T in T/P-BFO nanocomposites is obviously increased with increase in mole ratio percentage of T [21]. To investigate the morphology and microstructure of P-BFO and 9T/P-BFO nanocomposite, the TEM and HRTEM micrographs are taken. It can be seen clearly, that the P-BFO possesses random distribution with a particle size of about 100 nm as shown in Fig. 1A. Moreover, the nanocrystalline rhombohedral distorted structure of P-BFO is confirmed from the SAED pattern (inset of Fig. 1A). Fig. 1B and inset shows the TEM and HRTEM micrographs of 9T/P-BFO nanocomposite. In the HRTEM micrograph of 9T/P-BFO, the lattice fringes of (1 1 0) planes with inter-planar distance of 0.35 nm correspond to nanocrystalline $TiO_2$, whereas the inter-planar distance of 0.28 nm with (0 1 2) crystal planes correspond to P-BFO, indicating that an intimate interface junction exist between $TiO_2$ and P-BFO.

The UV–vis DRS spectra of P-BFO, T and T/P-BFO nanocomposites is given in (SFig. 1B). The corresponding band gaps of 3.2 eV for T and 2.07 eV for P-BFO were calculated by using equation Eg = 1240/λ [22]. In diffuse reflectance spectroscopy of T, the absorption edge lower than 400 is attributed to the electronic transition
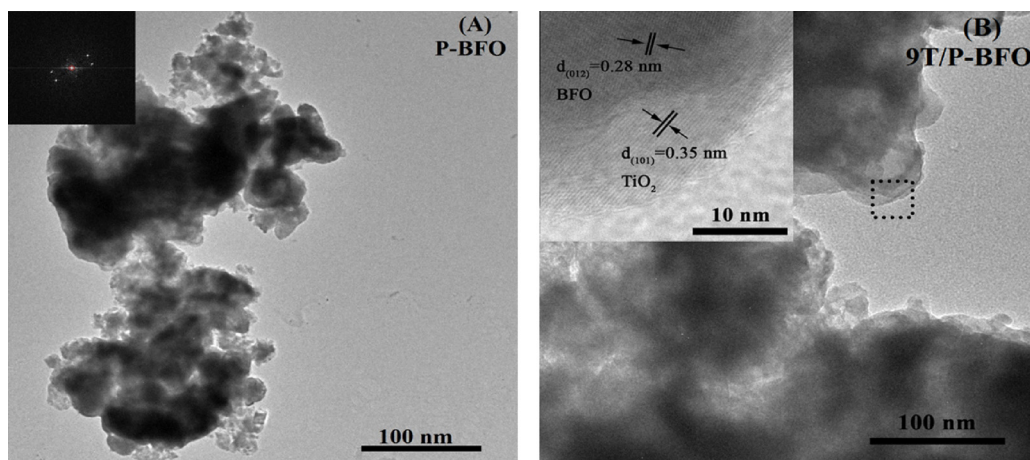
Fig. 1. TEM image of P-BFO with inset SAED patterns (A), and TEM image of 9T/P-BFO nanocomposite with inset HRTEM image (B).

from the valance band to the conduction band ($O2p \rightarrow Ti3d$) for anatase $TiO_2$ [21]. The UV–vis DRS spectrum of P-BFO annealed at 600 °C display two characteristic reflection regions, one from 500 to 700 nm and another from 700 to 800 nm. These reflection regions are attributed to the metal–metal transition and crystal field transitions, respectively [23].

The FT-IR spectra of the P-BFO, T and T/P-BFO nanocomposites are depicted in (SFig. 2). In the FT-IR spectra of P-BFO and T/P-BFO nanocomposites, the smaller peaks at 450 $cm^{-1}$ and the intense at 550 $cm^{-1}$, respectively, correspond to the bending and stretching vibrations of the Fe—O bonds. The bands at 1632 $cm^{-1}$ can be ascribed to the bending vibrations of the $H_2O$ molecules. While the broad bands at 3400–3600 $cm^{-1}$ are attributed to the bonds stretching in $H_2O$ and $^-OH$ groups, originated from the adsorbed $H_2O$ molecules from air [24]. In FTIR spectrum of $TiO_2$, the broad band at about 500–850 $cm^{-1}$ correspond to the stretching vibration mode of Ti—O—Ti in nanocrystalline anatase phase. In addition, all samples exhibit characteristic peaks at 1384 $cm^{-1}$, which correspond to the KBr diluents [25].

To further investigate the surface composition and chemical states of the as-prepared P-BFO and 9T/P-BFO nanocomposite, XPS measurements were conducted as shown in SFig. 3. For P-BFO, the XPS spectrum of Bi4f (SFig. 3A), exhibit two strong peaks at 163.88 eV and 158.57 eV, respectively, correspond to the ($Bi_{5/2}$) and ($Bi_{7/2}$). The Fe2p spectrum of P-BFO (SFig. 3B) also exhibit two bands at 723.61 eV and 710.28 eV. Moreover, the strong peak at 529.25 eV (SFig. 3C) corresponds to the lattice oxygen. In the XPS spectrum of 9T/P-BFO nanocomposite, a strong peak at 458.02 eV (S.Fig. 3D) is detected, which correspond to Ti2p. In addition, the XPS peaks are slightly shifted toward low binding energy, suggesting that an intimate contact exist between the interface of $TiO_2$ and P-BFO. [17,26] In general, the band bending at the interface mainly originates from the surface defects. Greater the surface defects at the interface of binary metal oxides, smaller will be the band bending and hence induces smaller conduction band offsets.

Fig. 2A shows the $N_2$ adsorption–desorption isotherms of P-BFO and 9T/P-BFO nanocomposite. It can be seen clearly, that P-BFO and 9T/P-BFO nanocomposite exhibit porous structure. The BET surface area of the 9T/P-BFO nanocomposite is (26.31 $m^2 g^{-1}$), which is higher than the unmodified P-BFO (20.28 $m^2 g^{-1}$). The pore size distributions of P-BFO and 9T/P-BFO nanocomposite is calculated from desorption branch by the Barrett–Joyner Halenda (BJH) method as shown in Fig. 2B. It is confirmed, that both the samples exhibit long and wide hysteresis loops, which are related to the disordered porous structure. Further, the disorderness of the porosity is confirmed by the low dV/dR values at BJH pore size distributions.

The pore diameter of P-BFO is apparently decreased from 26.7 to 15.47 nm after coupling with T. At low relative pressures, the isotherm exhibits like a sharp capillary condensation rung, which may be due to the small size pores ranging between 3 and 5 nm and the hysteresis loop formed at high relative pressures assigned to the large pores sizes above 10 nm range [27]. This difference in the surface area and pore structure would be reasonable for high photocatalytic performance.

### 3.2. Photogenerated charge transfer and separation

The surface photovoltage (SPV) is a potential method used to investigate the photo-induced charge transfer and separation properties of semiconducting materials and principally comprise SS-SPS and TS-SPV responses [28]. According to the SPS principles, the SPS responses for nanocrystalline semiconductors mainly derive from the photo-generated charge separation via diffusion process. This depends on the concentration of oxygen. The SPS responses of the unmodified P-BFO in different atmosphere and that of P-BFO and 9T/P-BFO nanocomposite in $N_2$ atmosphere were measured. From the SS-SPS response of P-BFO in $N_2$ environment (SFig. 4A), it can be observed that the unmodified P-BFO do not show obvious SPS response in $N_2$ environment, however, the SPS response is significantly enhanced in air and $O_2$ atmosphere, suggesting that the presence of $O_2$ is necessary for the SPS response to occur. Further, it is found that 9T/P-BFO nanocomposite (SFig. 4B) even exhibits an obvious SPS response in $N_2$ environment. Therefore, it is trust-worthy that the unexpected SPS response of 9T/BFO in $N_2$ environment is mainly attributed to the significantly improved separation of photogenerated charges as a result of unusual spatial transfer of visible-light induced high-energy electrons from P-BFO to $TiO_2$ [16].

The SS-SPS response peaks of P-BFO, $TiO_2$ and T/P-BFO nanocomposites in air atmosphere are shown in Fig. 3A. It can be seen clearly, that as the amount of coupled $TiO_2$ increases, the SS-SPS response peak intensity of P-BFO also increases. However, the excess amount of coupled $TiO_2$ hinders the charge transfer rate and hence the SS-SPS response peak decreases. The strongest SS-SPS response peak is observed for the 9T/P-BFO nanocomposite. Interestingly, the SS-SPS response peaks are in good agreement with the TS-SPV responses and PL peak intensities as follows. Based on the SS-SPS principles [29], the SPS responses for nanocrystalline material are equivalent to the quick TS-SPV responses. Hence, it is deduced that the separation of visible-light excited charge carriers is greatly improved.
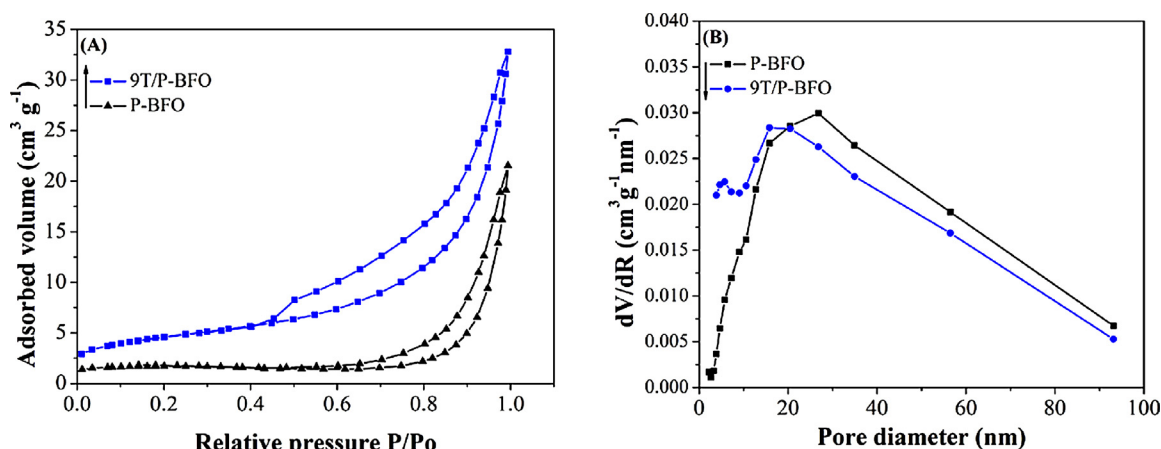
**Fig. 2.** N$_2$ adsorption/desorption isotherms (A) and Pore diameter (B) of P-BFO and 9T/P-BFO nanocomposite.

To further investigate the dynamic properties of the photo-generated charge carriers, the TS-SPV responses of the samples were measured under a laser pulse irradiation with a wavelength of 532 nm as shown in Fig. 3B. All the samples show positive TS-SPV responses. On the basis of these results, it is concluded that under 532 nm laser irradiation, the positive holes are produced and then collected on the testing electrode surface. The slow response mainly arises from the charge diffusion process and is positive in air due to the photo-induced electron captured by the adsorbed O$_2$, so that the holes diffuse to the surface of electrode preferentially. Hence, it is worthy of noting that the 9T/P-BFO nanocomposite exhibits longer lifetime of charge carrier and higher separation efficiency in comparison to the unmodified P-BFO alone.

The PL spectroscopy is a highly sensitive and non-destructive technique, widely used in the field of photocatalysis over semiconductors to investigate the electronic structure, optical and photochemical properties of active sites on the surface of metal oxides. From PL spectrum, we can get information about the surface defects and oxygen vacancies, as well as charge transfer, immigration and charge carrier trapping efficiency. Fig. 3C shows the PL spectra of P-BFO and T/P-BFO nanocomposites with the excitation wavelength of 325 nm. It is observed that the P-BFO and T/P-BFO nanocomposites exhibit strong PL signals (blue emission) at the wavelength range from 350 to 525 nm, which is mainly attributed to the electronic transitions from the conduction band of BFO to its valance band [30,31]. Generally speaking, lower the PL signal, lower the charge recombination rate and higher the separation efficiency. For 9T/P-BFO, the lowest PL signal is detected, indicating the high charge separation efficiency. Obviously, this is consistent among SS-SPS, TS-SPV and PL results.
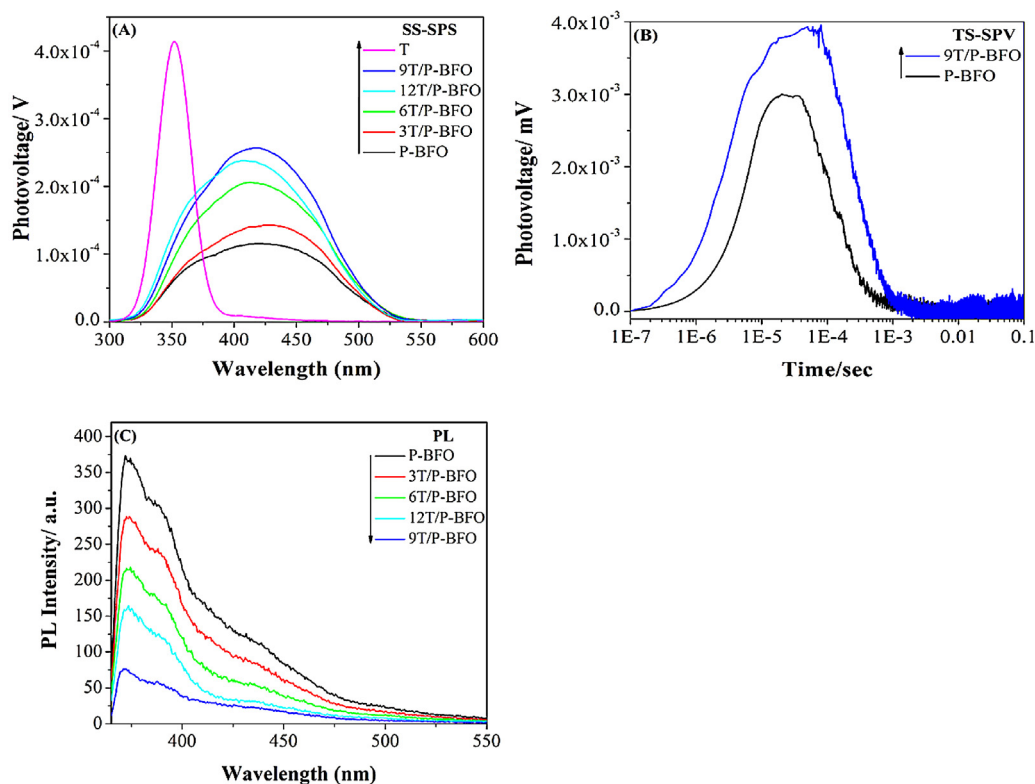


**Fig. 3.** SS-SPS responses of P-BFO and T/P-BFO nanocomposites (A), TS-SPV responses of P-BFO and 9T/P-BFO nanocomposite (B), and Photoluminescence (PL) spectra of P-BFO and T/P-BFO nanocomposites (C).
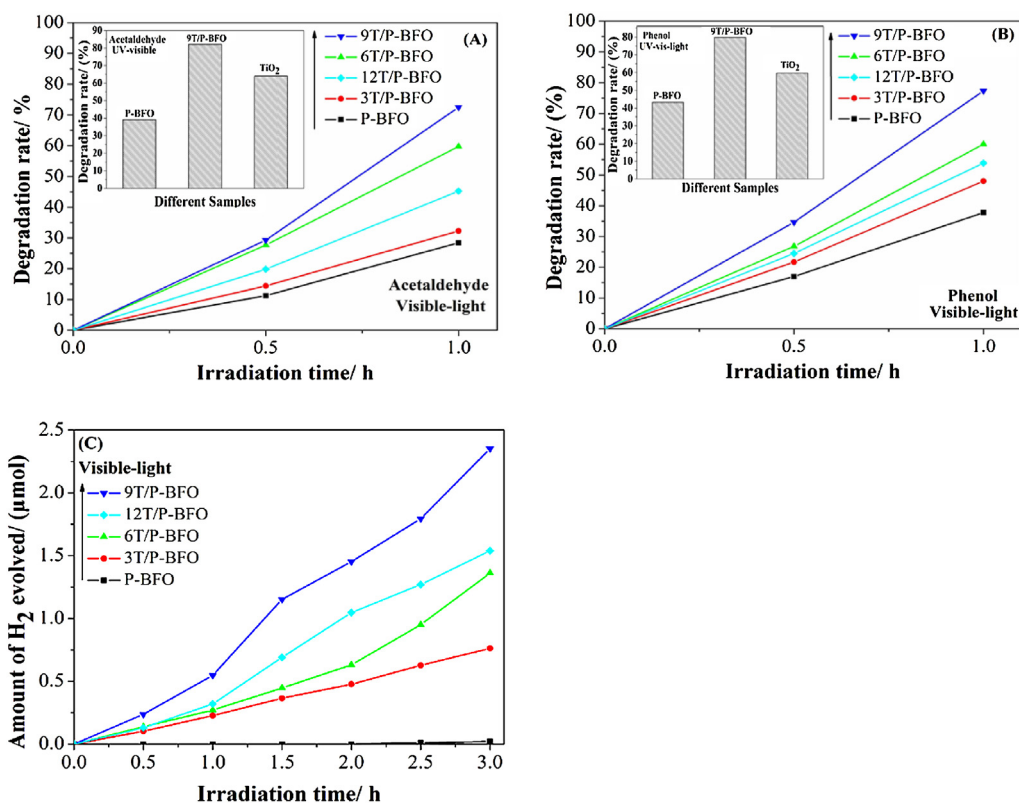
**Fig. 4.** Vis-light photocatalytic activity of P-BFO and T/P-BFO nanocomposites with inset UV–vis light photocatalytic activity of $TiO_2$, P-BFO and 9T/P-BFO nanocomposite for acetaldehyde degradation (A) and phenol degradation (B), Vis-light photocatalytic activity of P-BFO and T/P-BFO nanocomposites for $H_2$ production (C).

### 3.3. Visible-Light photoactivities

The visible light photocatalytic activities of P-BFO and T/P-BFO nanocomposites for acetaldehyde and phenol degradation were measured as shown in Fig. 4A and 4B, respectively. It can be seen clearly, that the photocatalytic degradation rates of P-BFO for acetaldehyde and phenol are greatly enhanced (about 2 times) after coupling with $TiO_2$, and 9T/P-BFO shows the best efficiency. It is trust-worthy that the enhanced photocatalytic activities are mainly attributed to the prolonged lifetime and the improved separation of photogenerated charges. To further prove the visible-light degradation activities of T/P-BFO, we have measured the photocatalytic activities of the as-synthesized $TiO_2$, P-BFO and 9T/P-BFO nanocomposite under UV–vis irradiation for acetaldehyde and phenol degradation as shown in the (inset of Fig. 4A and B), respectively. Compared with the visible-light photocatalytic activities of P-BFO and T/P-BFO, the UV–vis light ones are slightly enhanced. Interestingly, 9T/P-BFO exhibits high photocatalytic activity as compared to the as-synthesized $TiO_2$. Hence, it is suggested that the formed nanostructured heterojunction of binary oxides is more favorable for degradation of pollutants as compared to single semiconductor oxide, especially under visible irradiation.

Moreover, the visible-light photocatalytic activities of P-BFO and T/P-BFO nanocomposites for $H_2$ evolution were also measured as shown in Fig. 4C. It is observed that the photocatalytic activity of P-BFO is negligible for $H_2$ generation from the water–methanol mixture. However, the activity is obvious after coupling with nanocrystalline $TiO_2$. For BFO, a potential candidate for water oxidation, it is uncommon to photocatalytically generate $H_2$ in the aqueous-methanol system, even in the presence of Pt as a co-catalyst. Interestingly, it is demonstrated that the heterojunction T/P-BFO nanocomposite has the ability for water reduction. Herein, $0.8 \mu$ mol $h^{-1}$ $H_2$ is detected for 9T/P-BFO nanocomposite.

Therefore, it is confirmed that the resulting T/P-BFO nanocomposite could display good performance for photocatalytic water reduction to generate $H_2$ under visible light irradiation.

### 3.4. Discussion on mechanism

The coumarin fluorescent method was used to detect the amount of $OH^\bullet$ radicals produced as shown in (Fig. 5A), since it is widely accepted that the $OH^\bullet$ radicals play an active role in the photocatalytic degradation of pollutants. It can be seen clearly, that the fluorescence peak intensity gradually increases with increase in amount of $TiO_2$ coupled, and the strongest fluorescence peak intensity is observed for 9T/P-BFO nanocomposite. Therefore, it is suggested that the enhanced visible-light photocatalytic activities of T/P-BFO nanocomposites for acetaldehyde and phenol degradation are mainly attributed to the significant increase in amount of $OH^\bullet$ radicals produced [19,32].

The photocurrent densities of P-BFO and T/P-BFO nanocomposites under visible light irradiation and in dark were measured as shown in Fig. 5B and (SFig. 5), respectively. It can be seen that in dark, no photocurrent response is observed for all the samples but under visible light irradiation, the photocurrent response gradually increases as the amount of coupled $TiO_2$ increases. However, the excess amount of coupled $TiO_2$ leads to the decreased photocurrent response. The highest photocurrent response is observed for 9T/P-BFO nanocomposite at the applied voltage of $0.4$ V vs Ag/AgCl. It is expected that this decrease in photocurrent density is mainly attributed to the over excess amount of $TiO_2$ coupled, which covers the photocatalyst surface since the negligible photocurrent density is observed for $TiO_2$ under visible light irradiation.

In order to further prove the above results, the photocurrent action spectra (SFig. 6) as a function of visible-light excitation wavelengths ($\lambda \leq 600$ nm) at $0.4$ V bias vs. Ag/AgCl is measured for P-BFO,
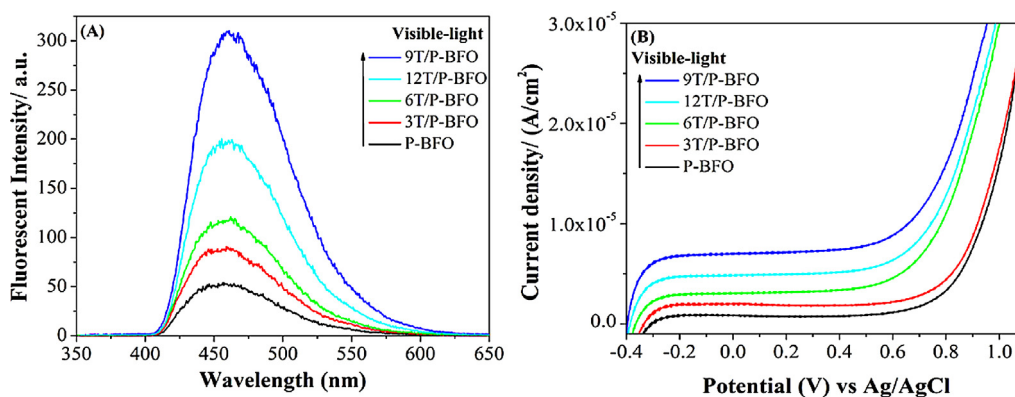
**Fig. 5.** OH• radical amount related Fluorescence spectra (A) and I–V curves (B) of P-BFO and T/P-BFO nanocomposites under visible light irradiation. PEC performance was measured in 1 mol L$^{-1}$ NaOH electrolyte solution. A three electrode cell was used with the testing film as the working electrode, an Ag/AgCl (saturated KCl solution) as a reference electrode, and Pt plate was used as counter electrode.

6T/P-BFO and 9T/P-BFO nanocomposites. For P-BFO, the photocurrent gradient keeps a relative smooth variation with decreasing the excitation wavelengths. However, for 6T/P-BFO and 9T/P-BFO, a significant enhancement in the photocurrent response is observed at wavelength ($\lambda \leq 500$ nm), which is closely related to the high energy level of photo-excited electrons. According to the UV–vis DRS spectra, the band gap of BFO is 2.07 eV, which can be excited by visible-light ($\lambda \leq 600$ nm). When T/P-BFO nanocomposite is irradiated under visible-light ($\lambda \leq 500$ nm) with photon energy higher than the CB of BFO, photogenerated high energy electrons are produced, which could transfer thermodynamically to the conduction band of TiO$_2$, so as to improve the separation of photogenerated charges. Naturally, by doing this, it is easy to make the photocatalytic water reduction more practical. These results are in good agreement with the above SS-SPS and TS-SPV responses, suggesting that the charge separation of P-BFO is significantly enhanced after coupling with a proper mole ratio percentage (9%) of TiO$_2$.

Based on the above results, it is well concluded that the visible light excited charge carrier's lifetime and separation efficiency of P-BFO could be increased after coupling with an appropriate amount of TiO$_2$, leading to the improved visible light photocatalytic activity for pollutant degradation and H$_2$ evolution. Hence, it is suggested that the enhanced efficiency is mainly attributed to the unusual spatial transfer of visible light excited high energy electrons of P-BFO to TiO$_2$. To understand the suggested mechanism, a possible energy level diagram for the T/P-BFO nanocomposites system is constructed as depicted in Fig. 6. According to the UV–vis DRS spectra for anatase TiO$_2$ (*n*-type semiconductor), the reported

band gap energy is 3.2 eV. The estimated work function is 4.2 eV and its Fermi level is about 0.2 eV, which lies below the bottom of conduction band [7]. BiFeO$_3$ is a p-type semiconductor [33–36], whose band gap varies from 2.0 to 2.7 eV and its Fermi level lies close to its valance band. Here the band gap of BFO is calculated to be 2.07 eV according to the UV–vis DRS spectra. The VB and CB position of TiO$_2$ and BFO at point of zero charge on standard hydrogen electrode scale (ca 4.5 eV) can be calculated by E$_{VB}$ = X − E$^e$ + 0.5 E$_g$ and E$_{CB}$ = E$_{VB}$ − E$_g$, respectively. Thus, the E$_{VB}$ levels for TiO$_2$ and BFO stand at 3.0 and 2.28 eV, respectively, and their E$_{CB}$ levels are positioned at −0.2 and +0.21 eV [17,37]. Thus, the energy gap (Eg) between the TiO$_2$ E$_{CB}$ and the BFO E$_{VB}$ is 2.48 eV, corresponding to the light energy of 500 nm by the equation: $\lambda$ = 1240/Eg. Interestingly, it is in good agreement with the photocurrent action spectroscopy result on the significant enhancement at wavelength ($\lambda \leq 500$ nm). This indicates that the produced high energy electrons of BFO excited by light with wavelength shorter than 500 nm would transfer thermodynamically to the CB of TiO$_2$. According to the schematic diagram, the visible-light in the wavelength range from 500 to 400 nm is favored for transfer of high-energy electrons from BFO to TiO$_2$. The light from 500 to 400 nm wavelength range accounts for 10.33% of the solar spectrum, therefore, it is expected that the fabricated T/P-BFO nanocomposite has a great potential for solar energy utilization. In fact, it is in good agreement with our previous work [16], in which, it is demonstrated that the visible-light excited energetic electrons would transfer thermodynamically from BiVO$_4$ to TiO$_2$, leading to the enhanced photoactivities.

Naturally, it is deduced that when heterojunction is formed between T and BFO, their Fermi energy levels tend to descend and rise up. At the same time, an electric field will be formed at the interface of the heterojunction nanocomposite system. At equilibrium position, negative charge will appear on P-BFO junction face while positive on TiO$_2$ junction face due to the formed interface electric field. Hence, it is believeable that when the T/P-BFO nanocomposite is irradiated under visible-light with the photon energy higher than the conduction band of P-BFO, the photoinduced high energy electrons are produced, which could transfer thermodynamically to the conduction band of TiO$_2$. Thus, the charge carrier's recombination significantly reduces, leading to the enhanced photocatalytic activities. On the other hand, the visible-light excited high energy electrons in unmodified P-BFO could easily be relaxed to the bottom of conduction band (CB) in extremely short period with energy loss, leading to the poor charge carriers separation and low photocatalytic activity. Hence, there is a great potential for solar energy consumption by the uncommon heterojunction nanocomposites. The as-synthesized T/P-BFO nanocomposites can be used
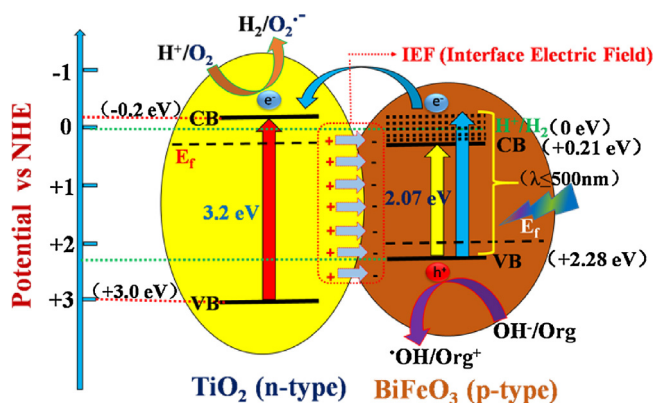


**Fig. 6.** Schematic diagram showing the energy band gaps of P-BFO and TiO$_2$ and the possible transfer mechanism of visible-light excited high energy electrons from BFO to TiO$_2$.

as visible-light responsive photocatalysts for potential applications in environmental protection and solar fuel production.

## 4. Conclusion

In summary, P-BFO and T/P-BFO nanocomposites have been successfully synthesized. Compared with the unmodified P-BFO, the T/P-BFO nanocomposites exhibit high photocatalytic activities for degradation of gas-phase acetaldehyde, the liquid-phase phenol and water splitting to evolve $H_2$ under visible light irradiation. It is concluded that when T/P-BFO nanocomposite is irradiated under visible-light ($\lambda \leq 500$) with photon energy higher than the conduction band of P-BFO, photogenerated charge carriers (electron–hole pairs) are produced and the high energy electrons could transfer thermodynamically to the conduction band of $TiO_2$ due to the built in electric field at the interface of nanocomposites. These significantly suppress the charge carrier's recombination and hence prolong its lifetime and improve its separation efficiency. The T/P-BFO nanocomposites display low charge carrier recombination, which shows promising applications in the field of photocatalysis for degrading pollutants and solar fuel production. This work is feasible to synthesize nanophotocatalysts based on P-BFO for efficient solar energy utilization, which are also applicable to other visible-light-responsive semiconducting composite nanomaterial.

## Acknowledgements

## Appendix A. Supplementary data

Supplementary data associated with this article can be found, in the online version, at http://dx.doi.org/10.1016/j.apcatb.2015.06.035

## References

[1] K. Maeda, K. Domen, J. Phys. Chem. 111 (2007) 7851–7861.
[2] T. Choi, S. Lee, Y.J. Choi, V. Kiryukhin, S.W. Cheong, Science 324 (2009) 63–66.
[3] R. Nechache, C. Harnagea, S. Licoccia, E. Traversa, A. Ruediger, F. Pignolet, A. Rosei, Appl. Phys. Lett. 98 (2011) 202902.
[4] F. Gao, Y. Yuan, K.F. Wang, X.Y. Chen, F. Chen, J.M. Liu, Z.F. Ren, Appl. Phys. Lett. 89 (2006) 102506.
[5] U.A. Joshi, J.S. Jang, P.H. Borse, J.S. Lee, Appl. Phys. Lett. 92 (2008) 242106.
[6] J.L.O. Quinonez, D. Dias, I.Z. Dbe, H.A. Santamaria, I. Betancourt, P.S. Jacinto, N.N. Etzana, Inorg. Chem. 52 (2013) 10306–10317.
[7] Y. Zhang, A.M. Schultz, P.A. Salvador, G.S. Rohrer, J. Mater. Chem. 21 (2011) 4168–4174.
[8] Z. Li, Y. Shen, C. Yang, Y. Lei, Y. Guan, Y. Lin, D. Liu, C.W. Nan, J. Mater. Chem. A 1 (2013) 823–829.
[9] K. Varaprasad, K. Ramam, G.S.M. Reddy, R. Sadiku, RSC Adv. 4 (2014) 60363–60370.
[10] J.J. An, L.H. Zhu, Y.Y. Zhang, H.Q. Tang, J. Environ. Sci. 25 (2013) 1213–1225.
[11] S. Li, J.M. Zhang, M.G. Kibria, Z. Mi, M. Chaker, D.L. Ma, R. Nechache, F. Rosei, Chem. Commun. 49 (2013) 5856–5858.
[12] J.J. Zhu, D.H. Mao, J. Li, X.F. Xie, X.G. Yang, Y.J. Wu, Mol. Catal. A: Chem. 233 (2005) 29–34.
[13] J. Xu, J. Liu, Z. Zhao, J. Zheng, G. Zhang, A. Duan, G. Jiang, Catal. Today 153 (2010) 136–142.
[14] B. Gao, J. Deng, Y. Liu, Z. Zhao, X. Li, Y. Wang, H. Dai, J. Chin. Catal. 34 (2013) 2223–2229.
[15] Y. Liu, H. Dai, Y. Du, J. Deng, L. Zhang, Z. Zhao, C.T. Au, J. Catal. 287 (2012) 149–160.
[16] M. Xie, X. Fu, L. Jing, P. Luan, Y. Feng, H. Fu, Adv. Energy Mater. 4 (2014) 1300995.
[17] Y.C. Yang, Y. Liu, J.H. Wei, C.X. Pan, R. Xiong, J. Shi, RSC Adv. 4 (2014) 31941–31947.
[18] A. Zhu, Q. Zhao, X. Li, Y. Shi, ACS Appl. Mater. Interfaces 6 (2014) 671–679.
[19] P. Luan, M. Xie, X. Fu, Y. Qu, X. Sun, L. Jing, Phys. Chem. Chem. Phys. 17 (2015) 5043–5050.
[20] L. Jing, Y. Qu, H. Su, C. Yao, H. Fu, j. Phys. Chem. C 115 (2011) 12375–12380.
[21] M. Sakar, S. Balakumar, P. Saravanan, S.N. Jaisankar, Mater. Res. Bull. 48 (2013) 2878–2885.
[22] W. Wang, L. Jing, Y. Qu, Y. Luan, H. Fu, Y. Xiao, J. Hazard. Mater. 243 (2012) 169–178.
[23] S. Li, Y.H. Lin, B.P. Zhang, J.F. Li, C.W. Nan, J. Appl. Phys. 105 (2009) 054310.
[24] N.I. Ilic, A.S. Dzunuzovic, J.D. Bobic, B.S. Stojadinovic, P. Hammer, M.M.V. Petrovic, Z.D.D. Mitrovic, B.D. Stojanovic, Ceram. Int. 41 (2015) 69–77.
[25] L. Jing, X. Qin, Y. Luan, Y. Qu, M. Xie, Appl. Surf. Sci. 258 (2012) 3340–3349.
[26] T. Gao, Z. Chen, Y.X. Zhu, F. Niu, Q.L. Huang, L.S. Qin, X.G. Sun, Y.X. Huang, Mater. Res. Bull. 59 (2014) 6–12.
[27] H. Su, L. Jing, K. Shi, C. Yao, H. Fu, J. Nanopart Res. 12 (2010) 967–974.
[28] L.Q. Jing, W. Zhou, G.H. Tian, H.G. Fu, Chem. Soc. Rev. 42 (2013) 9509–9549.
[29] L.M. He, L.Q. Jing, Y.B. Luan, L. Wang, H.G. Fu, ACS Catal. 4 (2014) 990–998.
[30] S.K. Mandal, T. Rakshit, S.K. Ray, S.K. Mishra, P.S.R. Krishna, A. Chandra, J. Phys. Condens. Matter. 25 (2013) 055303.
[31] D. Rajasree, G.K. Gobinda, V. Shikha, D.M. Goutam, M. Kalyan, J. Phys. Chem. C 117 (2013) 20209–20216.
[32] P. Luan, M. Xie, D. Liu, X. Fu, L. Jing, Sci. Rep. 4 (2015) 6180.
[33] B. Vengalis, J. Devenson, A.K. Oginskis, R. Butkut, A. Maneikis, A. Steik unien, L. Dapkus, M. Banys, J. Kinka, Acta Phys. Pol. A Vol. 113 (2008) 1095–1098.
[34] G.Z. Dong, H.Q. Fan, H.L. Tian, Q. Fang, J.W. Li, RSC Adv. 5 (2015) 29618–29623.
[35] N. Maso, A.R. West, Chem. Mater. 24 (2012) 2127–2132.
[36] N. Maso, H. Beltra, M. Prades, E. Cordoncillo, A.R. West, Phys. Chem. Chem. Phys. 16 (2014) 19408–19416.
[37] S.J.A. Moniz, R.Q. Cabrera, C.S. Blackman, J. Tang, P. Southern, P.M. Weaverd, C.J. Carmalt, J. Mater. Chem. A 2 (2014) 2922–2927.